



HNb_xTa_{1-x}WO₆ monolayer nanosheets solid solutions: Tunable energy band structures and highly enhanced photocatalytic performances for hydrogen evolution

Yuhao Liu^a, Jinhua Xiong^a, Yuying Yang^a, Shuiguang Luo^a, Shiyong Zhang^b, Yanhua Li^b, Shijing Liang^{a,*}, Ling Wu^{a,*}

^a State Key Laboratory of Photocatalysis on Energy and Environment, Fuzhou University, Fuzhou 350002, PR China

^b Hunan Province Key Laboratory of Applied Environmental Photocatalysis, Changsha University, Changsha 410022, PR China

ARTICLE INFO

Article history:

Received 6 June 2016

Received in revised form 17 August 2016

Accepted 24 October 2016

Available online 28 October 2016

Keywords:

HNb_xTa_{1-x}WO₆ nanosheets

Solid solutions

Band energy

Photocatalytic

Hydrogen evolution

ABSTRACT

HNb_xTa_{1-x}WO₆ monolayer nanosheets solid solutions were successfully synthesized through a top-down method. The crystal structure and morphology of the prepared materials were investigated by X-ray diffraction patterns (XRD), Raman spectra, and transmission electron microscopy (TEM). Atomic force microscopy (AFM) further confirmed that the thicknesses of the nanosheets solid solutions were at a range of 1.50–2.00 nm. As the ratios of Nb increased from $x = 0.0$ to 1.0 in HNb_xTa_{1-x}WO₆ nanosheets solid solutions, the photo-absorption spectra were red-shifted, showing a decrease in the band gaps (from 3.26 to 3.10 eV), and the flat band potentials were shifted positively (from -0.78 to -0.68 eV). The photocatalytic activities of hydrogen evolution from water for these samples were found to be strongly dependent on their composition, which would increase as the mole ratios of Nb to Ta increases. Among the prepared nanosheets solid solutions, HNb_{0.7}Ta_{0.3}WO₆ nanosheets showed the highest photocatalytic activity for H₂ evolution with a rate constant of $1320.0 \mu\text{mol h}^{-1} \text{g}^{-1}$. Combining with the photo-electrochemical analyses, precise control of the energy band structure via a solid solution strategy is a useful method for band engineering to develop an efficient photocatalyst.

© 2016 Elsevier B.V. All rights reserved.

1. Introduction

Hydrogen as a renewable and sustainable form of energy has drawn dramatically increasing attention due to clean emission and high conversion efficiencies [1,2]. Photocatalytic H₂ generation from water by using solar energy provides an alternative environmentally friendly way, but the key is to develop highly active and stable photocatalysts [3–5]. Among them, many layered compounds have shown great photocatalytic performance of hydrogen evolution from water splitting [6]. While the layered precursors suffer from high charge density between the layers, narrow layer spacing and shielded reaction sites, limiting their further promotion of photocatalytic performances for hydrogen evolution.

Recently, two-dimensional (2D) transition metal oxides nanosheets with molecular thickness are emerging as important novel photocatalysts because of their particular structural properties, such as high surface area, anisotropic features, and

single-crystalline texture [7–9]. These nanosheets with various nanostructures can be fabricated from different elemental compositions of layered precursors, which are another attractive aspects of nanosheets [10]. Recently, many groups have reported that HCa₂Nb₃O₁₀, HSR₂Nb₃O₁₀, HLaNb₂O₇, HTiNbO₅, SnNb₂O₆, H₄Nb₆O₁₇ and HNb₃O₈ nanosheets with 1–2 nm thickness show photocatalytic activities [11–16]. The photocatalytic performance of these given materials are strongly dependent on their structural features and physicochemical properties [17]. Thus, precise control of the energy band structure is essential to understanding the influence of structure on the activity at a molecular level.

The solid solution strategy as a useful band engineering method has been used to enhance the photocatalytic activity of a given semiconductor photocatalyst. For example, a solid solution of GaN and ZnO with a band gap of 2.58–2.76 eV can achieve water splitting into H₂ and O₂ under visible light irradiation, whereas the band gaps of GaN and ZnO are about 3.4 and 3.2 eV, respectively [18]. Following this research line, a novel highly active solid-solution photocatalyst (Ag_{0.75}Sr_{0.25})(Nb_{0.75}Ti_{0.25})O₃ with a band gap of 2.8 eV has been developed for efficient decomposition of organic pollutants under visible-light irradiation [19]. Recently,

* Corresponding authors.

E-mail addresses: sjliang2011@gmail.com (S. Liang), wuling@fzu.edu.cn (L. Wu).

Domen et al. found that $\text{BaZrO}_3\text{--BaTaO}_2\text{N}$ solid solutions having a band gap of 1.7–1.8 eV can realize both photocatalytic reducing and oxidizing water under irradiation above 660 nm [20]. This band engineering method has usually been used for designing bulk-type semiconductor materials. However, how the energy band structure affects the photocatalytic performance of monolayer nanosheets via a solid solution strategy remains little explored. The lack of such information limits further development of a highly active photocatalyst based on nanosheets.

Herein, monolayer $\text{HNb}_x\text{Ta}_{1-x}\text{WO}_6$ nanosheets solid solutions with different energy band structures were successfully prepared through a top-down method. The crystal structures, morphologies, photoabsorption performances, electronic structure properties, and photocatalytic activities of the prepared materials with different mole ratios of Nb to Ta were further investigated. Furthermore, the origin of enhanced activity was analyzed from photoelectrochemical measurements. Our current work can provide a feasible way for tuning monolayer nanosheets photoabsorption and photocatalytic properties from the molecular level.

2. Experiment section

2.1. Materials and reagents

All chemicals associated were reagent grade and were used without further purification: lithium carbonate (Li_2CO_3 , A.R., Sinopharm Chemical Reagent Co. (SCRC)), niobium oxide (Nb_2O_5 , SCRC), tantalum oxide (Ta_2O_5 , SCRC), tungsten trioxide (WO_3 , SCRC), nitric acid (HNO_3 , 65–68.0 wt%, SCRC), triethanolamine (TEOA, SCRC), $\text{H}_2\text{PtCl}_6\cdot 6\text{H}_2\text{O}$ (SCRC), deionized water.

2.2. Preparation of monolayer $\text{HNb}_x\text{Ta}_{1-x}\text{WO}_6$ nanosheets

Layered $\text{HNb}_x\text{Ta}_{1-x}\text{WO}_6$ ($x = 0.0, 0.3, 0.5, 0.7$, and 1.0) was prepared by proton-exchange of the precursors $\text{LiNb}_x\text{Ta}_{1-x}\text{WO}_6$. Layered $\text{LiNb}_x\text{Ta}_{1-x}\text{WO}_6$ was obtained by calcination stoichiometric amounts of WO_3 , Nb_2O_5 , Ta_2O_5 and Li_2CO_3 at 1033–1073 K for 48 h with one intermediate grinding. The proton exchange reaction for the generation of layered $\text{HNb}_x\text{Ta}_{1-x}\text{WO}_6\cdot 1.5\text{H}_2\text{O}$ was carried out in an aqueous solution of nitric acid (4 M) at a given temperature for six days. During the proton exchange reaction, the acid solution was replaced with a fresh one every two days. The $\text{HNb}_x\text{Ta}_{1-x}\text{WO}_6$ sample was then washed thoroughly with distilled water and dried in air at 333 K. The nanosheets suspensions were obtained by adding 80.0 mg layered $\text{HNb}_x\text{Ta}_{1-x}\text{WO}_6$ into 80.0 mL 10 vol.% TEOA aqueous solution under continuous stirring, as reported previously [21]. The supernatant solutions containing the nanosheets were collected by centrifuging. The addition of HNO_3 aqueous solution (1.0 M, 100 mL) to 100 mL of the nanosheets solution resulted in immediate aggregation of the nanosheets as a precipitate. The aggregated samples, $\text{HNb}_x\text{Ta}_{1-x}\text{WO}_6$ nanosheets ($\text{NS-HNb}_x\text{Ta}_{1-x}\text{WO}_6$), were then rinsed three times with 100 mL of 0.5 M HNO_3 aqueous solution to remove amine and with a large amount of distilled water to remove HNO_3 and finally were dried at 333 K in a vacuum oven.

2.3. Characterization

X-Ray diffraction (XRD) patterns were carried on a Bruker D8 Advance X-ray diffractometer operated at 40 kV and 40 mA with Nifiltered Cu K α irradiation ($\lambda = 0.15406$ nm). The data were recorded in the 2θ range of 5–40°. Raman spectroscopic measurements were performed on a Renishaw inVia Raman System 1000 with a 532 nm Nd:YAG excitation source at room temperature. X-ray photoelectron spectroscopy (XPS) measurements were performed on a PHI Quantum 2000 XPS system with a monochromatic

Al K α source and a charge neutralizer. The element content of the sample was monitored by Inductively Coupled Optical Emission Spectrometer (ICP-OES) on Optima 8000 (PerkinElmer). Before ICP-OES experiment, the solid sample was digested in mixture of HNO_3 and HF. Transmission electron microscopy (TEM) images were measured using a JEOL model JEM2010 EX microscope at an accelerating voltage of 200 kV. A tapping-mode atomic force microscopy (AFM, Nanoscope Multimode IIIa, Veeco Instruments) with Si-tip cantilever was used to evaluate the morphology of the obtained nanosheets on the mica substrate. UV–vis diffuse reflectance spectra (UV–vis DRS) were obtained by a Cary 500 UV–vis–NIR spectrophotometer. The photocurrent was measured by a conventional three-electrode electrochemical cell with a working electrode, a platinum foil counter electrode and Ag/AgCl as a reference. The photocurrent measurements were conducted with a BAS Epsilon workstation. A 300 W Xenon lamp was used as a light source. Electrochemical Impedance Spectroscopy (EIS) experiments and the Mott-Schottky analyses were carried out on a ZENNIUM electrochemical workstation (Zahner, Germany).

2.4. Evaluation of photocatalytic activity

The photocatalytic H_2 evolution activity was evaluated in an air-tight gas recirculation system equipped with an inner irradiation quartz reaction cell. Typically, 80.0 mg of layered $\text{HNb}_x\text{Ta}_{1-x}\text{WO}_6$ were added into 80.0 mL 10 vol.% TEOA aqueous solutions under continuous stirring to obtain $\text{NS-HNb}_x\text{Ta}_{1-x}\text{WO}_6$ dispersions, then in-situ reaction with simulated sunlight irradiation (Fig. S1, Supporting information). 1.0 wt% of Pt co-catalyst was loaded on the surface of nanosheets through the in-situ photodeposition method using $\text{H}_2\text{PtCl}_6\cdot 6\text{H}_2\text{O}$ as the precursor [22]. The suspension was then thoroughly degassed to remove dissolved air and irradiated by a 300 W Xenon lamp (PLS-SXE300C, Perfectlight Co., Beijing). The reactant solution was stirred and maintained at room temperature by a flow of cooling water during the photocatalytic reaction. The amount of evolved H_2 was detected by an online gas chromatograph (Shanghai Precision Scientific Instrument Co, Ltd, GC112A, TCD, Ar carrier).

3. Results and discussion

Fig. 1 shows XRD patterns of layered $\text{LiNb}_x\text{Ta}_{1-x}\text{WO}_6$, $\text{HNb}_x\text{Ta}_{1-x}\text{WO}_6$ and $\text{NS-HNb}_x\text{Ta}_{1-x}\text{WO}_6$ materials. From Fig. 1a, the samples of $x = 0.0$ and 1.0 show the single-phase diffraction pattern assigned to layered LiTaWO_6 and LiNbWO_6 , respectively. The replacement of Nb^{5+} in Ta^{5+} site is theoretically not expected to cause a significant perturbation since the effective ionic radius of Nb^{5+} and Ta^{5+} is the same 0.064 nm when the coordination number is 6 [23]. Nevertheless, the (110) and (103) diffraction peaks of the prepared samples undergo angle shift as the Nb content increasing, indicate that the $\text{LiNb}_x\text{Ta}_{1-x}\text{WO}_6$ solid solutions were formed. Different from the layered parent compounds (Fig. 1b), the $\text{NS-HNb}_x\text{Ta}_{1-x}\text{WO}_6$ obtained by virtue of TEOA aqueous solution (Fig. 1c) just exhibited a few very weak and broad diffraction peaks because of the turbostratic disorder restacking and the loss of the periodicity in c axial. These diffractions peaks shifted to lower angles than the corresponding (002) peaks in layered $\text{HNb}_x\text{Ta}_{1-x}\text{WO}_6$. Relatively intense (110) and (200) diffractions peaks, resulting from in-plane lattice directions, are preserved. The distinct shift of (110) diffraction peaks for $\text{NS-HNb}_x\text{Ta}_{1-x}\text{WO}_6$ were observed in the enlarged view of the spectra (Fig. 1d). These features suggest that the $\text{NS-HNb}_x\text{Ta}_{1-x}\text{WO}_6$ solid solutions were successfully prepared.

Raman spectroscopy is a powerful technique that allows the local structure of solid materials to be examined. The Raman

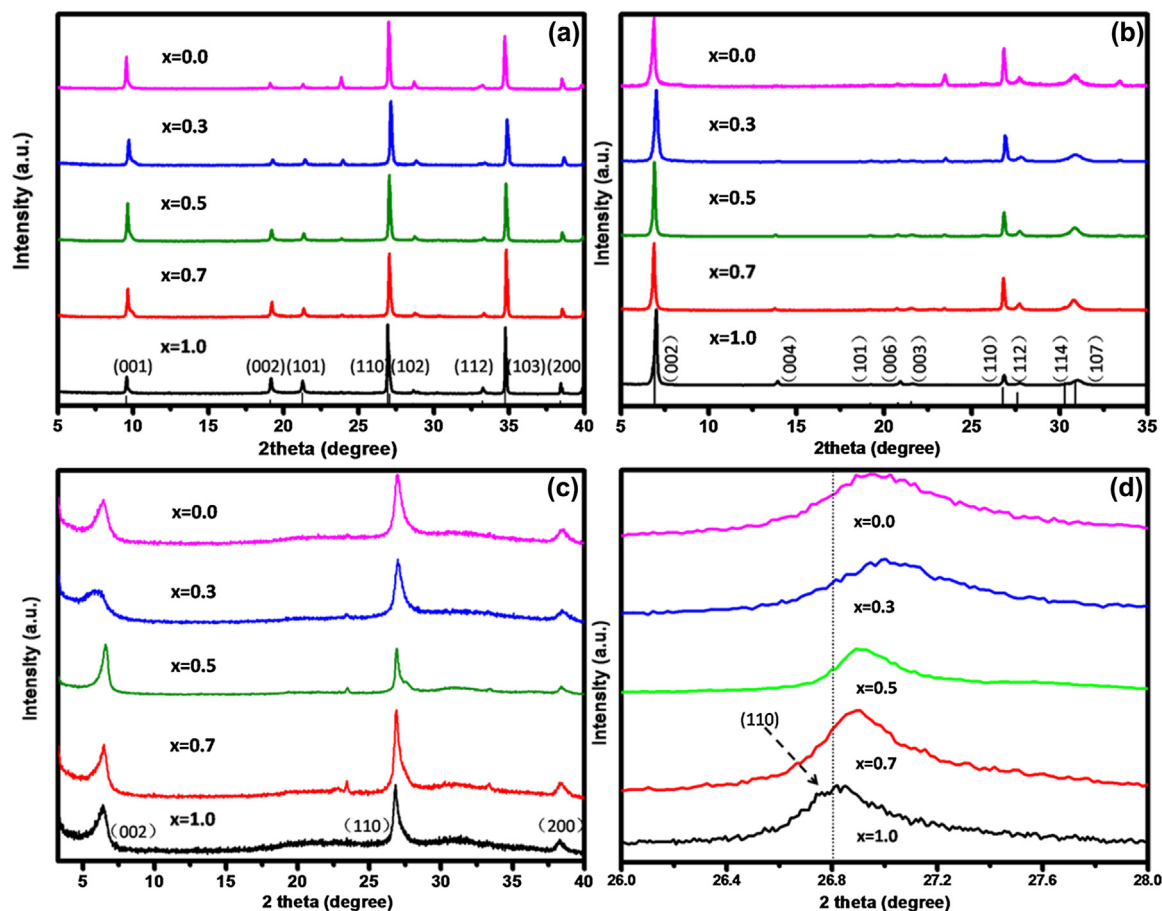


Fig. 1. XRD patterns of layered $\text{LiNb}_x\text{Ta}_{1-x}\text{WO}_6$ (a), $\text{HNb}_x\text{Ta}_{1-x}\text{WO}_6$ (b) and $\text{NS-HNb}_x\text{Ta}_{1-x}\text{WO}_6$ (c), (d) a magnified view of the (110) diffraction peak of $\text{NS-HNb}_x\text{Ta}_{1-x}\text{WO}_6$ ($x=0.0, 0.3, 0.5, 0.7, 1.0$).

spectra of the $\text{NS-HNb}_x\text{Ta}_{1-x}\text{WO}_6$ are presented in Fig. 2a. All of the samples presented almost the same Raman vibration peaks at around 990–980, 910–900, 615–605, 460–450, 370–360, and 230–220 cm^{-1} . The assignments of the Raman bands are possible according to previous work on the corresponding layered materials [24,25]. With increasing the Nb content (x), however, the Raman peaks of the ν ($\text{M}=\text{O}$) and δ ($\text{O}-\text{M}-\text{O}$) ($\text{M}=\text{Nb}/\text{Ta}$) for $\text{NS-HNb}_x\text{Ta}_{1-x}\text{WO}_6$ shifted to lower wave numbers were observed in the enlarged view of the spectra (Fig. 2b). According to Hardcastle and Wachs's empirical equation of ν

(cm^{-1}) = $25922\exp(-1.9168 \cdot R)$, where ν is the $\text{M}-\text{O}$ stretching wavenumber and R is the $\text{M}-\text{O}$ bond length, the average bond length of $\text{M}-\text{O}$ becomes longer with the x value increasing [20]. Therefore, the various mole ratios of Nb to Ta in $\text{NS-HNb}_x\text{Ta}_{1-x}\text{WO}_6$ solid solutions will lead to pronounced (or shrinkage) distortion of the layers that consist of MO_6 octahedron. The results of Raman further confirm that the $\text{NS-HNb}_x\text{Ta}_{1-x}\text{WO}_6$ solid solutions were successfully synthesized.

X-ray photoelectron spectroscopy (XPS) was performed to determine the chemical compositions and the valence states of

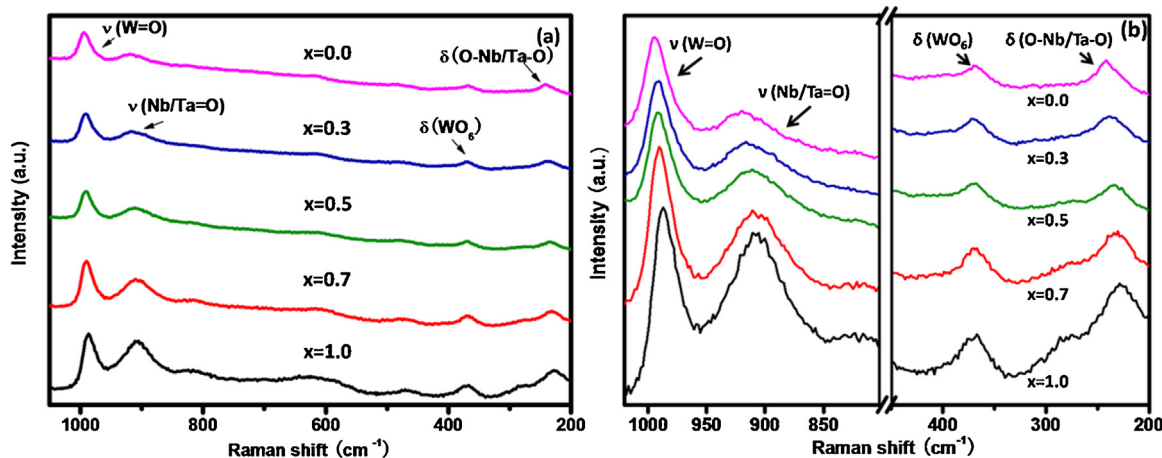


Fig. 2. Raman spectra of $\text{NS-HNb}_x\text{Ta}_{1-x}\text{WO}_6$ (a) ($x=0.0, 0.3, 0.5, 0.7, 1.0$), (b) a magnified view of the main peaks.

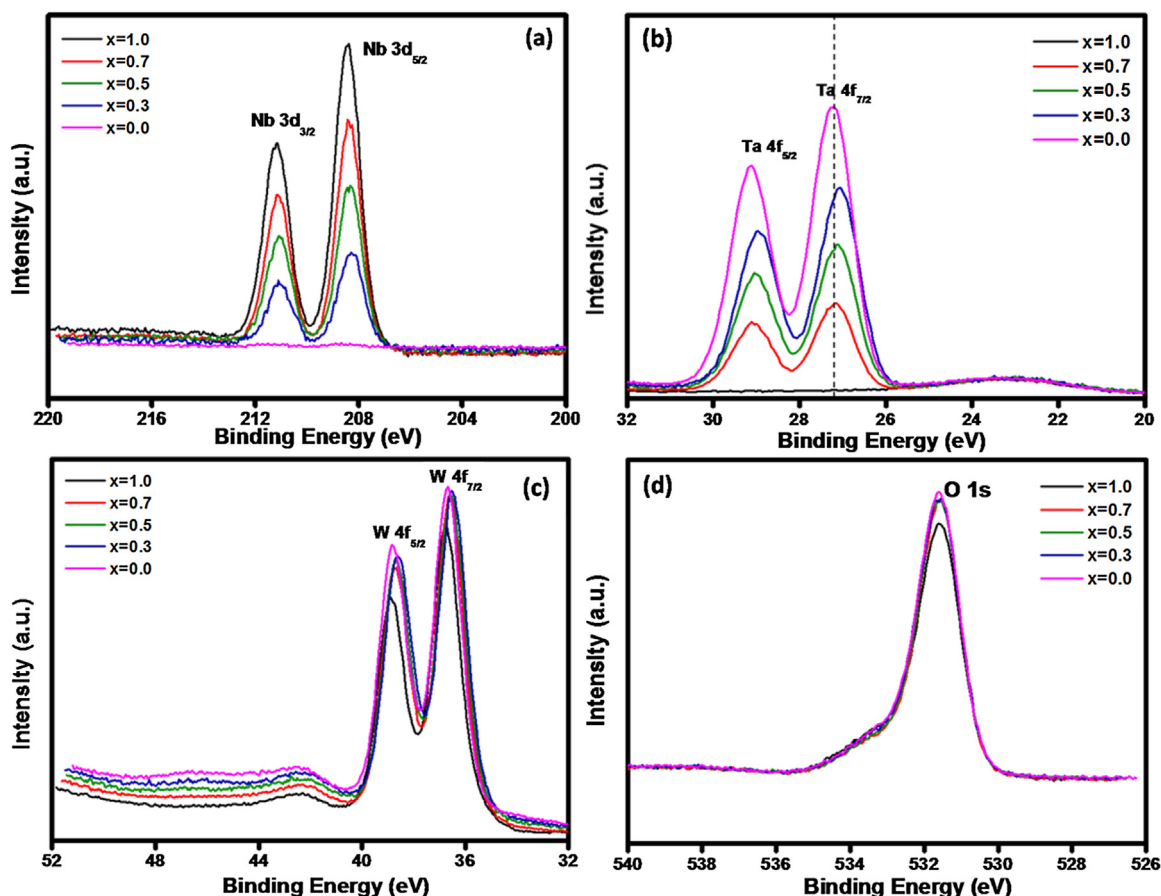


Fig. 3. High-resolution XPS spectra of NS-HNb_xTa_{1-x}WO₆ ($x = 0.0, 0.3, 0.5, 0.7, 1.0$).

the prepared samples. Fig. 3 shows high-resolution XPS spectra of four elements for NS-HNb_xTa_{1-x}WO₆ solid solutions. For the Nb 3d spectrum, the spin orbit separation of Nb 3d_{3/2} is located at around 211.2 eV and the Nb 3d_{5/2} peak appears at 208.4 eV, corresponding to Nb⁵⁺ in an octahedral structure (Fig. 3a). Also, the Ta 4f_{5/2} and Ta 4f_{7/2} peaks were centered at 29.1 and 27.2 eV with a spin-orbit separation of 1.9 eV (Fig. 3b). These peaks can be assigned to Ta⁵⁺ of NS-HNb_xTa_{1-x}WO₆ solid solutions. The W 4f_{5/2} and 4f_{7/2} peak were observed at 38.8 and 36.6 eV, respectively (Fig. 3c), corresponding to W⁶⁺ of the prepared materials. Similarly, the O 1s XPS spectrum (Fig. 3d) showed narrow peaks with a binding energy of 531.6 eV and slight asymmetry. These peaks were attributed to the M–O (M = Nb/Ta) in NS-HNb_xTa_{1-x}WO₆ and H₂O or OH groups on the surface of the samples [26]. The XPS data of O 1s, Nb 3d, Ta 4f and W 4f in NS-HNb_xTa_{1-x}WO₆ solid solutions are consistent, suggesting that each valence state of the four elements in these materials are same. Compared with the pristine HTaWO₆ nanosheets, the binding energies of Ta 4f in NS-HNb_xTa_{1-x}WO₆ solid solutions shift to much lower binding energies. The electron density decrease of Ta⁵⁺ due to the introduction of niobium atom in the host sheets [27]. Meanwhile, Table 1 shows the atomic ratios of Nb/Ta calculated from the XPS and ICP-AES for NS-HNb_xTa_{1-x}WO₆ solid solutions. The measured atomic compositions approximately equal to the nominal value. Thus, these data clearly indicate that NS-HNb_xTa_{1-x}WO₆ solid solutions can be successfully prepared in these ranges.

The morphologies of NS-HNb_xTa_{1-x}WO₆ solid solutions were confirmed by TEM images from Fig. 4. Representative TEM images showed in Fig. 4 reveal that the NS-HNb_xTa_{1-x}WO₆ solid solutions are nearly transparent with lateral scale ranging from submicrometer to several micrometers. These results indicate that the differences of x have negligible influence on the lateral dimensions.

AFM images further show that the as-prepared samples have 2D nanosheets structures and smooth surfaces (Fig. 5). The thicknesses of the HNb_{0.7}Ta_{0.3}WO₆ and HTaWO₆ nanosheets are 1.70 ± 0.05 nm and 1.50 ± 0.05 nm, respectively. These results well matched the thickness of the HNbWO₆ nanosheets (1.8–2.0 nm) [21], indicating that the as-prepared NS-HNb_xTa_{1-x}WO₆ solid solutions were monolayer.

The UV/Vis diffuse reflectance spectra (DRS) of NS-HNb_xTa_{1-x}WO₆ solid solutions are shown in Fig. 6. All samples exhibit absorption bands at around 380–400 nm. The positions of the absorption edge for NS-HNb_xTa_{1-x}WO₆ shift to longer wavelengths (red shift) with increased the x value. The band gaps (E_{BG}) were decreased from 3.26 eV (for $x = 0.0$) to 3.10 eV (for $x = 1.0$), which were estimated by linear extrapolation from the inflection point of the curve to the baseline. These results suggest that the changing of atomic composition via the solid solution strategy can affect the optical light absorption properties of the nano-materials.

Table 1
Atomic compositions of NS-HNb_xTa_{1-x}WO₆ ($x = 0.0, 0.3, 0.5, 0.7, 1.0$).

Entry	Nominal value	Atomic composition ^a n(Nb)/n(Ta)	Atomic composition [wt%] ^b		
			Nb	Ta	n(Nb)/n(Ta)
1	HNbWO ₆	1/0	23.2	0.0	1/0
2	HNb _{0.7} Ta _{0.3} WO ₆	0.68/0.32	16.5	14.1	0.69/0.31
3	HNb _{0.5} Ta _{0.5} WO ₆	0.48/0.52	10.0	18.5	0.51/0.49
4	HNb _{0.3} Ta _{0.7} WO ₆	0.27/0.73	9.1	29.4	0.38/0.62
5	HTaWO ₆	0/1	0.0	39.8	0/1

^a Mole ratios of Nb to Ta calculated by XPS.

^b Measured by ICP.

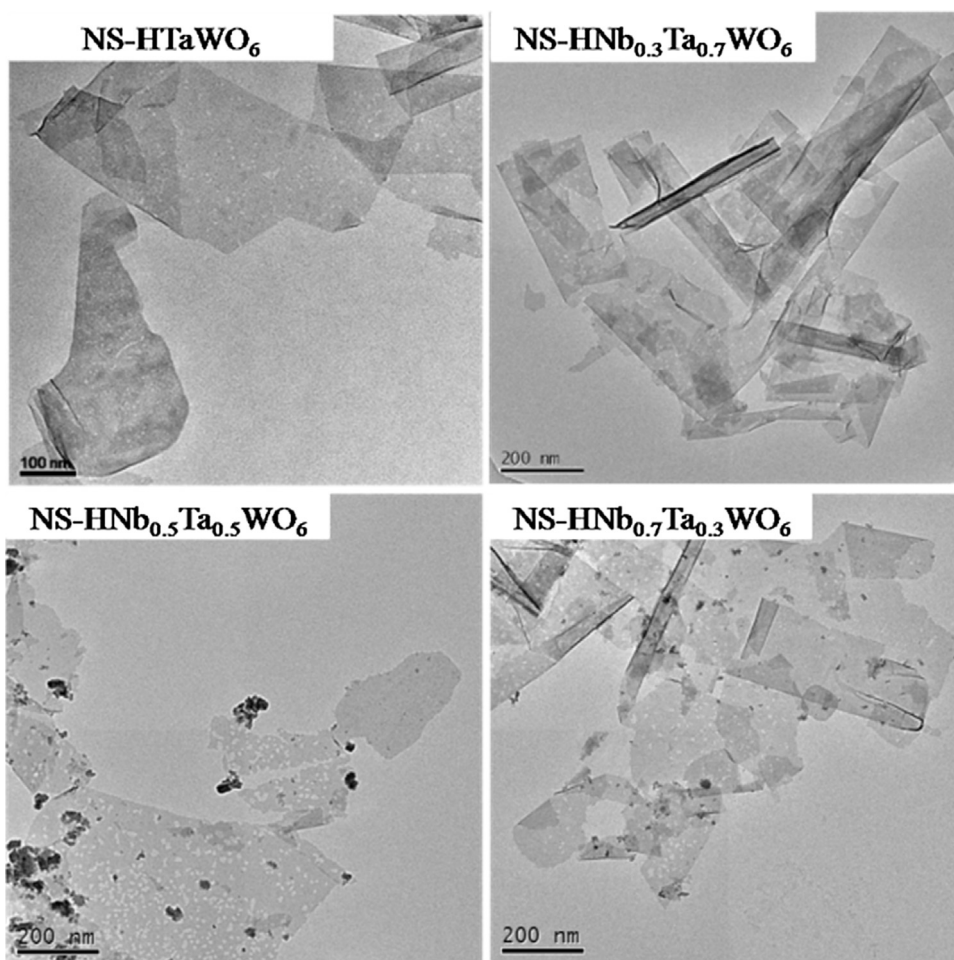


Fig. 4. TEM images of NS-HNb_xTa_{1-x}WO₆ (x = 0.0, 0.3, 0.5, 0.7).

In general, the valence band (VB) of the transition metal oxide is made up of O2p orbit. The conduction band (CB) is consists of the d orbitals of transition metal. The electronic nucleophilic potential of transition metal can be regarded as the judgment of the bottom of

the conduction band [28]. Therefore, metal oxides containing Ta⁵⁺ ions as the principal cationic component always have a more negative conduction band potential than those containing principally Nb⁵⁺ [29,30]. From these discussions, the change of band-gap with

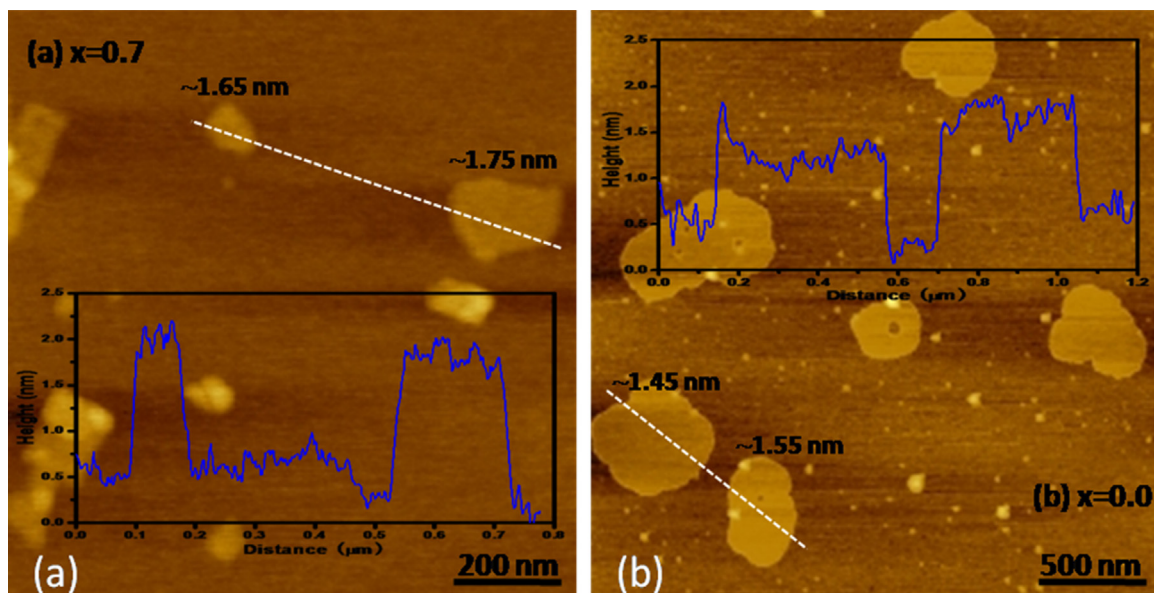


Fig. 5. AFM images of NS-HNb_xTa_{1-x}WO₆ (x = 0.0, 0.7).

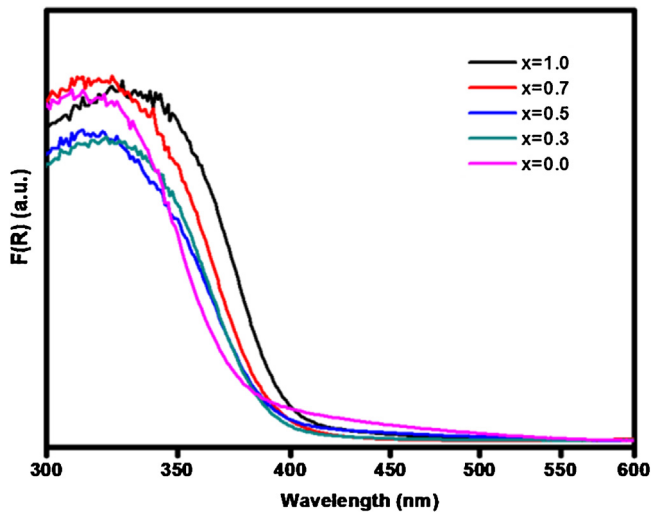


Fig. 6. UV/Vis diffuse reflectance spectra of NS-HNb_xTa_{1-x}WO₆ ($x = 0.0, 0.3, 0.5, 0.7, 1.0$).

various compositions may be caused by the difference of conduction band potential.

To better clarify the electronic structure properties of NS-HNb_xTa_{1-x}WO₆ solid solutions, Mott–Schottky measurements have been carried out. As displayed in Fig. 7, the flat band potentials (E_{FB}) of NS-HNb_xTa_{1-x}WO₆ are ca. -0.98 eV, -0.94 eV, -0.92 eV, -0.91 eV vs Ag/AgCl at pH=6.8 when $x = 0.0, 0.3, 0.5, 0.7$, respectively. For the n-type semiconductor, the CB bottom is near the flat band potential. The transform formula of flat band potentials

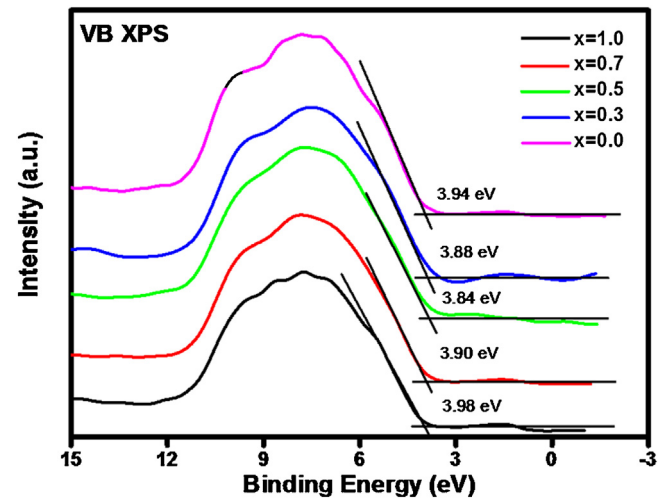


Fig. 8. VB XPS spectra of NS-HNb_xTa_{1-x}WO₆ ($x = 0.0, 0.3, 0.5, 0.7, 1.0$).

versus Ag/AgCl electrode and normal hydrogen electrode was as follow: $\varphi(\text{NHE}) = \varphi(\text{Ag/AgCl}) + 0.2$ eV. Therefore, the CB bottom of NS-HNb_xTa_{1-x}WO₆ are ca. -0.78 eV, -0.74 eV, -0.72 eV, -0.71 eV vs NHE (Normal Hydrogen Electrode) at pH=6.8 when $x = 0.0, 0.3, 0.5, 0.7$, respectively. The VB top of NS-HNb_xTa_{1-x}WO₆ could be investigated directly by valence band X-ray photoelectron spectroscopy (VB-XPS) (Fig. 8). The prepared samples displayed the characteristic VB density of states (DOS) with the edge of the maximum energy at about 3.94 eV, 3.88 eV, 3.84 eV, 3.90 eV, 3.98 eV below the Fermi energy when $x = 0.0, 0.3, 0.5, 0.7, 1.0$, respectively.

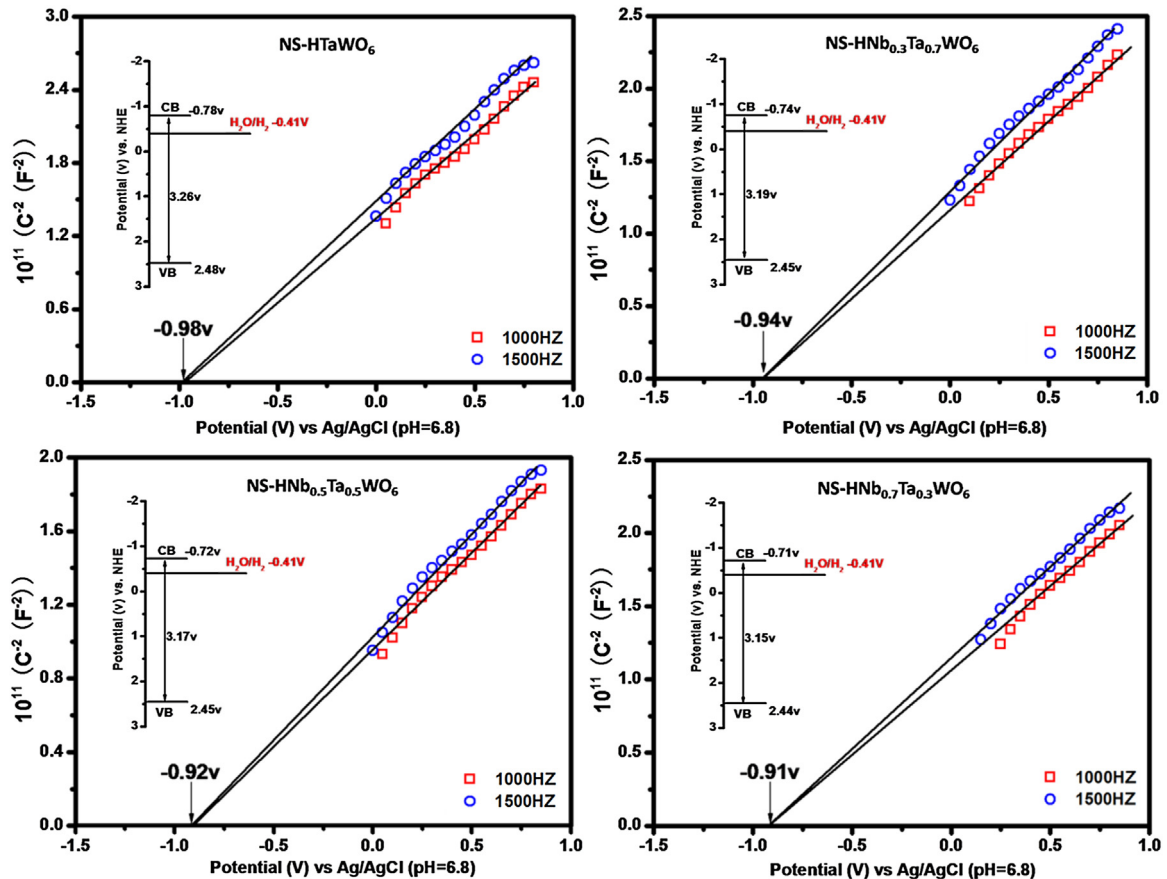


Fig. 7. Typical Mott–Schottky plots of NS-HNb_xTa_{1-x}WO₆ ($x = 0.0, 0.3, 0.5, 0.7$) in 0.2 M Na₂SO₄ aqueous solution (pH = 6.8).

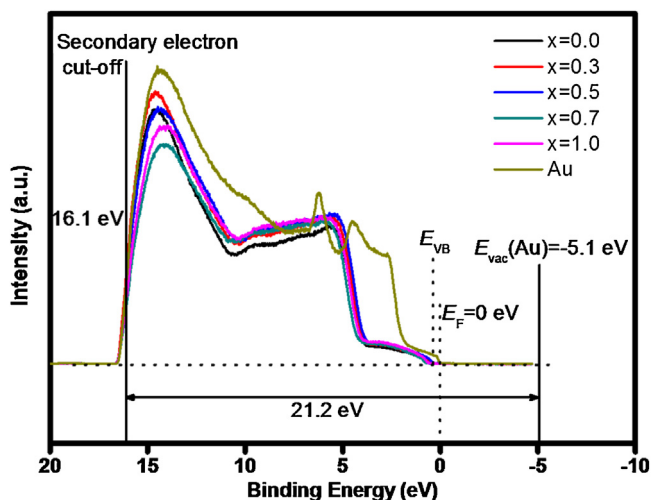


Fig. 9. UPS spectra of NS-HNb_xTa_{1-x}WO₆ ($x=0.0, 0.3, 0.5, 0.7, 1.0$) and Au.

Meanwhile, for the NS-HNb_xTa_{1-x}WO₆ solid solutions ($x=0.3, 0.5, 0.7$), the VB maximum energy down-shifts compared with that of HNbWO₆ and HTaWO₆ nanosheets. Compared with the VB-XPS, the ultraviolet photoelectron spectroscopy (UPS) using He (21.2 eV) as the excitation source, only making valence electrons ionization, thus can be used for further study the valence electrons and band structures of the samples. The relationship between several energy levels (E_{VB} (the valence band), E_F (the Fermi level), and E_{vac} (the vacuum level)) and the UPS spectrum of NS-HNb_xTa_{1-x}WO₆ and Au are shown in Fig. 9. The figure shows the scale of binding energy with the Fermi level of Au set at 0 V. The vacuum level (E_{vac}) should be located 21.2 eV above the cutoff energy of the spectrum. The work function of Au based on this definition is estimated to be 5.1 eV, that is, E_F is -5.1 eV with respect to E_{vac} , which is in agreement with the literature [31]. Fig. 10 shows a series of UPS spectra for NS-HNb_xTa_{1-x}WO₆ in the valence band regions. In this figure, the spectra were compared with $E_{vac}=0$ eV at the same position. The position of the top of the valence band (E_{VB}) for each sample is indicated on the spectrum. The difference between E_F and E_{VB} is determined by the intersection of the linear portion of the spectra near the Fermi edge (low binding energy region) with the baseline (Fig. 10). The E_{VB} is 0.47 eV, 0.44 eV, 0.40 eV, 0.61 eV, 0.56 eV when

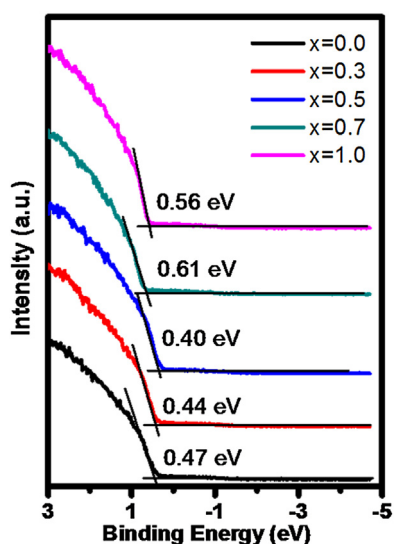


Fig. 10. UPS spectra of NS-HNb_xTa_{1-x}WO₆ in the valence band region ($x=0.0, 0.3, 0.5, 0.7, 1.0$).

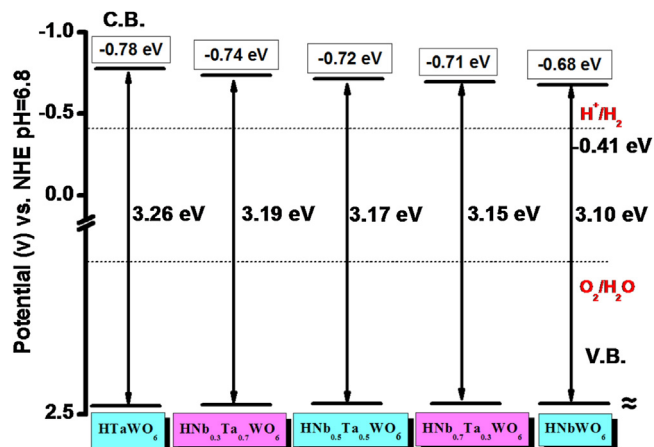


Fig. 11. A schematic illustration of band structures of NS-HNb_xTa_{1-x}WO₆ ($x=0.0, 0.3, 0.5, 0.7, 1.0$).

$x=0.0, 0.3, 0.5, 0.7, 1.0$, respectively. Therefore, their valence band maximum E_{VB} is -5.57 eV, -5.54 eV, -5.50 eV, -5.71 eV, -5.66 eV, respectively, with respect to E_{vac} . There are slight differences in VB top value for each sample. Furthermore, the results of VB top obtained from VB-XPS and UPS prove that the band structure of nanosheets can be effectively controlled via the solid solution strategy.

Based on the discussions of the UV-vis diffuse reflectance spectra and electrochemical analysis, the band structures of these nanosheets are schematically illustrated in Fig. 11. As the ratio of Nb was increased from $x=0.0$ to 1.0 in NS-HNb_xTa_{1-x}WO₆ solid solutions, the band gaps were significantly decreased (from 3.26 eV to 3.10 eV), indicating the light adsorption performances were on a steady rise. Meanwhile, the conduction band potentials of the samples were shifted positively (from -0.78 eV to -0.68 eV) under the same conditions. The potentials of the conduction band edge are more negative than the water reduction potential (-0.41 eV), suggesting that it is thermodynamically permissible for the transformation of photo-generated electrons into H₂O to produce H₂.

3.1. Photocatalytic properties

The effect of different compositions on photocatalytic properties were examined by the photocatalytic H₂ evolution from water over as-synthesized highly dispersed NS-HNb_xTa_{1-x}WO₆ solid

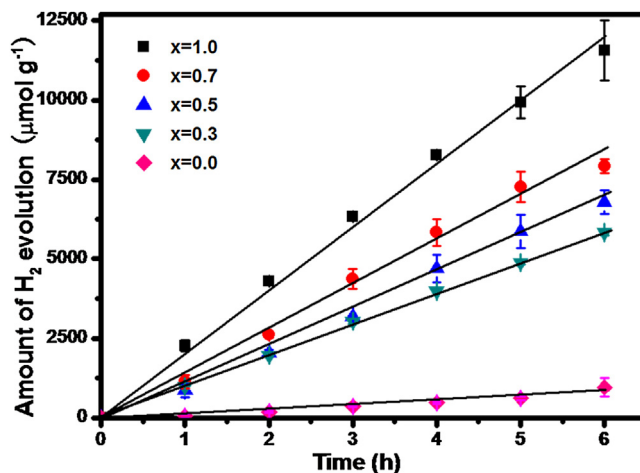


Fig. 12. Time course of H₂ evolved from water splitting using NS-HNb_xTa_{1-x}WO₆ ($x=0.0, 0.3, 0.5, 0.7, 1.0$).

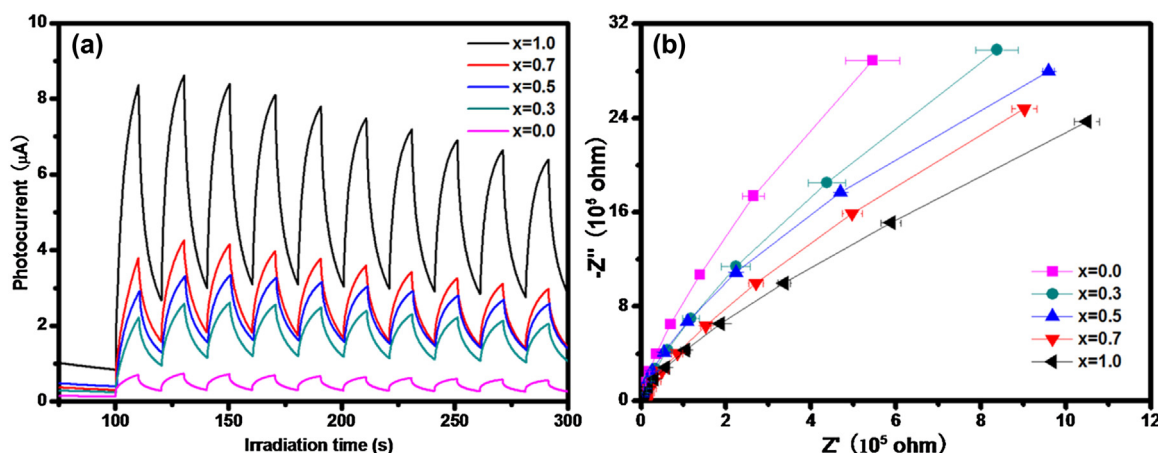


Fig. 13. Transient photocurrent response vs time profiles of NS-HNb_xTa_{1-x}WO₆ ($x=0.0, 0.3, 0.5, 0.7, 1.0$) (a), Electrochemical impedance spectroscopic Nyquist plots were obtained with various HNb_xTa_{1-x}WO₆ nanosheets photoelectrodes ($x=0.0, 0.3, 0.5, 0.7, 1.0$) (b).

solutions under simulated sunlight irradiation. As shown in Fig. 12, all materials exhibit reasonable activity; the performances tend to rise with increasing the x value; the amount of H₂ produced increased linearly with reaction time. The rate constants of photocatalytic hydrogen evolution from water follow the order: $x=1.0$ ($1927.5 \mu\text{mol h}^{-1} \text{g}^{-1}$) $> x=0.7$ ($1320.0 \mu\text{mol h}^{-1} \text{g}^{-1}$) $> x=0.5$ ($1131.3 \mu\text{mol h}^{-1} \text{g}^{-1}$) $> x=0.3$ ($972.5 \mu\text{mol h}^{-1} \text{g}^{-1}$) $> x=0.0$ ($160.0 \mu\text{mol h}^{-1} \text{g}^{-1}$). Based on the results of crystal structure, morphology and electronic structure property, the photocatalytic activity of each sample seems to be related to its energy band.

Since the energy band of photocatalysts have a close relationship to the photogenerated charge carriers, electrochemical methods were used for further analysis. The value of the photocurrent tends to indirectly reflect the semiconductor's ability to generate and transfer the photogenerated charge carrier under irradiation [32,33]. The magnitude of the photocurrent represents the charge collection efficiency of the electrode surface. Fig. 13a shows photocurrents generated from NS-HNb_xTa_{1-x}WO₆ films under 300 W xenon lamp excitations. All electrodes were prompt in generating photocurrent with a reproducible response to on-off cycles. The results of photocurrent are as follow: $x=1.0 > x=0.7 > x=0.5 > x=0.3 > x=0.0$, which confirmed the carrier separation ability of $x=1.0 > x=0.7 > x=0.5 > x=0.3 > x=0.0$. This order is consistent with the result of photocatalytic activity.

To further understand the essential difference of the photocatalytic performance for NS-HNb_xTa_{1-x}WO₆ solid solutions, we performed the electrochemical impedance spectroscopy (EIS) experiments. The smaller size of the arc in an EIS Nyquist plot indicates the smaller resistance at the interface and the smaller charge-transfer resistance on the electrode surface [34]. As shown in Fig. 13b, the radiuses of curvature for these samples were decreased with the x values increasing, indicated that the efficiencies of charge separation were increased. All of these results are in agreement with the report that the photocatalytic activities fluctuate depending on the various compositions.

In isostructural compounds such as solid solutions, the photocatalytic activity for H₂ evolution from water containing sacrificial electron donors generally increases with the conduction band edge potential [11,35]. Nevertheless, the samples of NS-HNb_xTa_{1-x}WO₆ with more positive conduction band edge potentials exhibit much better activity. As the value of x increases, the band gaps in NS-HNb_xTa_{1-x}WO₆ decreased, which were corresponding to the positive impact on photoabsorption abilities. Presumably, the wider absorption band of HNb_{0.7}Ta_{0.3}WO₆ nanosheets makes up for its slightly more positive conduction band edge potential in determining the overall yield of H₂ evolution. This phenomenon is in

agreement with the previous report on Ga_{2-x}In_xO₃ solid solutions as photocatalysts [11,36]. Combining with photoelectrochemical analyses, it is thus possible that the change of energy band structure via the solid solution strategy can affect the charge separation and/or charge transport process, resulting in different photocatalytic activities.

4. Conclusions

In summary, we successfully prepared monolayer HNb_xTa_{1-x}WO₆ nanosheets solid solutions for the first time with tunable band energy structure. The photocatalytic hydrogen evolution activities for these samples were found to be strongly dependent on the compositions. As the increasing of x values from 0.0 to 1.0, the corresponding activities were growing from only $160.0 \mu\text{mol h}^{-1} \text{g}^{-1}$ to $1927.5 \mu\text{mol h}^{-1} \text{g}^{-1}$. Moreover, the difference of photocatalytic performances can be explained by improved charge separations and much smaller resistances at the surface of samples via the solid solution strategy. This work could provide new insight in the exploration and utilization of the 2D nanosheets as well as the development of property-controllable synthesis of photocatalysts on the molecular level.

Acknowledgments

This work was supported by the National Natural Science Foundation of China (51672048 and 21677036), the China Postdoctoral Science Foundation (2015M571963) and the Natural Science Foundation of Fujian Province (2014J05016 and 2015YZ0001). S. Liang also thanks the Natural Science Funds for Distinguished Young Scholar of Fujian Province (2016J06004) and the University Distinguished Young Research Talent Training Program of Fujian Province.

Appendix A. Supplementary data

Supplementary data associated with this article can be found, in the online version, at <http://dx.doi.org/10.1016/j.apcatb.2016.10.077>.

References

- [1] K. Maeda, K. Teramura, D. Lu, T. Takata, N. Saito, Y. Inoue, K. Domen, *Nature* 440 (2006), 295–295.
- [2] L. Zhu, M. Hong, G.W. Ho, *Nano Energy* 11 (2015) 28–37.
- [3] R. Sasaki, K. Maeda, Y. Kako, K. Domen, *Appl. Catal. B* 128 (2012) 72–76.

- [4] L. Shen, M. Luo, Y. Liu, R. Liang, F. Jing, L. Wu, *Appl. Catal. B* 166 (2015) 445–453.
- [5] T.-F. Yeh, S.-J. Chen, H. Teng, *Nano Energy* 12 (2015) 476–485.
- [6] Y. Miseki, H. Kato, A. Kudo, *Energy Environ. Sci.* 2 (2009) 306–314.
- [7] X. Cai, T.C. Ozawa, A. Funatsu, R. Ma, Y. Ebina, T. Sasaki, *J. Am. Chem. Soc.* 137 (2015) 2844–2847.
- [8] L. Wang, T. Sasaki, *Chem. Rev.* 114 (2014) 9455–9486.
- [9] R. Ma, T. Sasaki, *Adv. Mater.* 22 (2010) 5082–5104.
- [10] K. Maeda, M. Eguchi, T. Oshima, *Angew. Chem. Int. Ed.* 53 (2014) 13164–13168.
- [11] K. Maeda, T.E. Mallouk, *J. Mater. Chem.* 19 (2009) 4813–4818.
- [12] Z. Zhai, X. Yang, L. Xu, C. Hu, L. Zhang, W. Hou, Y. Fan, *Nanoscale* 4 (2012) 547–556.
- [13] S. Liang, S. Zhu, Y. Chen, W. Wu, X. Wang, L. Wu, *J. Mater. Chem.* 22 (2012) 2670–2678.
- [14] M.C. Sarahan, E.C. Carroll, M. Allen, D.S. Larsen, N.D. Browning, F.E. Osterloh, *J. Solid State Chem.* 181 (2008) 1678–1683.
- [15] S. Liang, L. Wen, S. Lin, J. Bi, P. Feng, X. Fu, L. Wu, *Angew. Chem. Int. Ed.* 53 (2014) 2951–2955.
- [16] J. Xiong, L. Wen, F. Jiang, Y. Liu, S. Liang, L. Wu, *J. Mater. Chem. A* 3 (2015) 20627–20632.
- [17] S. Ida, T. Ishihara, *J. Phys. Chem. Lett.* 5 (2014) 2533–2542.
- [18] K. Maeda, T. Takata, M. Hara, N. Saito, Y. Inoue, H. Kobayashi, K. Domen, *J. Am. Chem. Soc.* 127 (2005) 8286–8287.
- [19] D. Wang, T. Kako, J. Ye, *J. Am. Chem. Soc.* 130 (2008) 2724–2725.
- [20] K. Maeda, K. Domen, *Angew. Chem. Int. Ed.* 51 (2012) 9865–9869.
- [21] Y. Liu, J. Xiong, S. Luo, R. Liang, N. Qin, S. Liang, L. Wu, *Chem. Commun.* 51 (2015) 15125–15128.
- [22] G. Zhang, M. Zhang, X. Ye, X. Qiu, S. Lin, X. Wang, *Adv. Mater.* 26 (2014) 805–809.
- [23] R.D. Shannon, *Acta Crystallogr. Sect. A* 32 (1976) 751–767.
- [24] S.-H. Byeon, H.-J. Nam, *Chem. Mater.* 12 (2000) 1771–1778.
- [25] J.M. Jehng, I.E. Wachs, *Chem. Mater.* 3 (1991) 100–107.
- [26] L. Wu, C.Y. Jimmy, X. Fu, *J. Mol. Catal. A: Chem.* 244 (2006) 25–32.
- [27] A. Dutta, S. Saha, P. Kumari, T. Sinha, S. Shannigrahi, *J. Solid State Chem.* 229 (2015) 296–302.
- [28] M. Oshikiri, M. Boero, J. Ye, Z. Zou, G. Kido, *J. Chem. Phys.* (2002) 117.
- [29] K. Maeda, *J. Photochem. Photobiol. C: Photochem. Rev.* 12 (2011) 237–268.
- [30] A. Kudo, Y. Miseki, *Chem. Soc. Rev.* 38 (2009) 253–278.
- [31] W.-J. Chun, A. Ishikawa, H. Fujisawa, T. Takata, J.N. Kondo, M. Hara, M. Kawai, Y. Matsumoto, K. Domen, *J. Phys. Chem. B* 107 (2003) 1798–1803.
- [32] M. Kong, Y. Li, X. Chen, T. Tian, P. Fang, F. Zheng, X. Zhao, *J. Am. Chem. Soc.* 133 (2011) 16414–16417.
- [33] Q. Xiang, J. Yu, M. Jaroniec, *J. Phys. Chem. C* 115 (2011) 7355–7363.
- [34] T. Xu, L. Zhang, H. Cheng, Y. Zhu, *Appl. Catal. B* 101 (2011) 382–387.
- [35] I. Tsuji, H. Kato, H. Kobayashi, A. Kudo, *J. Am. Chem. Soc.* 126 (2004) 13406–13413.
- [36] A. Kudo, I. Mikami, *J. Chem. Soc. Faraday Trans.* 94 (1998) 2929–2932.